Design and experimental demonstration of feedback adaptive RMP ELM controller toward complete long pulse ELM suppression on KSTAR

View Online   Export Citation   CrossMark

R. Shousha,[1,2,a] S. K. Kim,[1,2] K. G. Erickson,[2] S. H. Hahn,[3] A. O. Nelson,[4] S. M. Yang,[2] J.-K. Park,[2] J. Wai,[1,2] Y. M. Jeon,[3] J. H. Lee,[3] J. Jang,[3] D. Seo,[3] and E. Kolemen[1,2]

AFFILIATIONS

[1] Department of Mechanical and Aerospace Engineering, Princeton University, Princeton, New Jersey 08544, USA
[2] Princeton Plasma Physics Laboratory (PPPL), Princeton, New Jersey 08543, USA
[3] Korea Institute of Fusion Energy (KFE), Daejeon 34133, Republic of Korea
[4] Department of Applied Physics and Applied Mathematics, Columbia University, New York, New York 10027, USA

Note: This paper is part of the Special Collection: Papers from the 63rd Annual Meeting of the APS Division of Plasma Physics.
Note: Paper UI1 5, Bull. Am. Phys. Soc. **66** (2021).
[a] Invited speaker. **Author to whom correspondence should be addressed:** rshousha@princeton.edu

ABSTRACT

Operation of a fusion power plant requires robust edge localized mode (ELM) suppression simultaneously with high plasma performance. In this paper, we describe a novel feedback adaptive resonant magnetic perturbation (RMP) ELM controller designed to address this problem by achieving optimized ELM suppression through the advanced application of 3D RMPs. From real-time D_α data, the controller is able to achieve robust ELM suppression while simultaneously minimizing the applied RMP in order to enhance plasma performance. In real-time, the instantaneous ELM-frequency is analyzed with an adaptive feedback algorithm to determine amplitudes and phases of RMP coil currents that will maximize plasma performance while maintaining ELM suppression. When applied through the KSTAR plasma control system in several experiments using $n = 1$ RMPs, robust ELM suppression is achieved and sustained in feedback while reducing the RMP strength to $\sim$65% of its initial value. Minimization of the RMP strength in this manner not only allows for operation of longer discharges due to a decrease in flux consumption but also allows for a strong recovery of up to $\sim$60% of β_N throughout the ELM-free period.

I. INTRODUCTION

The discovery of H-mode—a plasma state bifurcation that occurs when sufficient external heating is applied, resulting in more stored energy per amount of external heating[1]—enabled a significant increase in efficiency compared to traditional L-mode plasmas, thereby providing a potential path to efficient fusion energy generation. As such, the ITER project will rely on H-mode operation to achieve performance milestones,[2] including the demonstration of a fusion power multiplication of $Q_{DT} = 10$. However, operating a plasma in the H-mode is not without risk, as the plasma tends to become unstable when performance is maximized.

When the plasma enters the H-mode, an edge transport barrier (ETB) with steep pressure gradients is formed, allowing the core pressure to increase significantly. However, the steepness of this gradient is limited by the destabilization of so-called edge localized modes (ELMs), which are typically observed in H-mode plasmas as violent expulsions of particles and energy from the plasma to the wall.[3] After an ELM, pressure gradients that were relaxed by the ELM crash increase again to meet the peeling–ballooning instability limit, creating a periodic phenomenon. In full performance ITER discharges, the transient heat load caused by the energy released in a single ELM on the divertor target plates is expected to exceed divertor material limits.[2,4] Therefore, it is crucial to develop ELM control techniques that can mitigate the deleterious effects of ELMs while still maximizing fusion performance in high power H-modes.

Multiple approaches to ELM mitigation in H-mode plasmas that utilize external controls have been investigated in the literature, including impurity seeding,[5–7] the injection of supersonic molecular

beams,[8–10] the use of small periodic vertical equilibrium displacements,[11,12] the application of low recycling wall materials,[13–15] periodic cryogenic pellet injections,[16,17] the application of lower hybrid waves,[18] and the application of specific edge resonant 3D magnetic perturbations (RMPs),[19–24] among others. While most of these approaches are aimed at limiting transient heat loads by triggering smaller ELMs at higher frequencies, the application of RMPs is designed to achieve and sustain complete ELM suppression.[19,23,25,26] In this approach, an applied RMP induces additional edge transport, causing a reduction in the pedestal height and, thus, lowering the pedestal gradient. The reduced gradient prevents access to the peeling–ballooning instability limit and thereby fully suppresses any potential ELM events. Extensive prior research into RMP induced transport has revealed that the additional diffusion process consists of contributions by both collisional[27–31] and turbulent[32–38] transport channels. However, while RMP-driven transport facilitates ELM suppression, it also constrains plasma performance via deterioration of global confinement as well as reduction of the pedestal height. In order for devices like ITER to be able to meet all of their performance objectives in an ELM suppressed regime, it is highly desirable to optimize the applied RMP in order to minimize the deleterious effect it usually has on plasma performance parameters.

One candidate approach to optimized RMP ELM suppression is to exploit a salient hysteresis phenomenon that has been observed in earlier experiments.[39] It has been found that for a given toroidal mode number of the RMP, the RMP amplitude at which ELM suppression is *lost* is lower than the RMP amplitude required to *access* the ELM suppressed regime. In addition, plasma performance parameters, such as confinement, are seen to recover when the applied RMP is reduced once the ELM suppressed regime has been entered. By implication, this hysteresis phenomenon could, thus, be used in a feedback ELM controller to enhance plasma performance under sustained ELM suppression. However, it is not yet possible to accurately predict the minimum required RMP needed to sustain ELM suppression.

Until models are developed that can accurately predict the minimum required RMP in real-time, an adaptive controller designed to exploit this hysteresis effect is needed. Such a controller would, by necessity, be comprised of several state machines, which dictate different dynamic behaviors of the requested RMP depending on the plasma conditions and controller settings. For RMP amplitude feedback control, a simple controller would ramp up the RMP amplitude until ELM suppression has been achieved, and then ramp down until ELM suppression is lost again. By repeatedly entering and losing ELM suppression, the optimal amplitude could potentially be determined. The success of this method is contingent on the assumption that the required RMP converges within the discharge (i.e., the RMP amplitude required for accessing and sustaining ELM suppression should converge). Since this assumption is not generally known to be true, the hysteresis phenomenon could lead to oscillatory behavior of the controller during iterations, which forms a significant obstacle to control convergence. Therefore, ELM control using such an adaptive scheme, becomes non-trivial.

This paper reports on the development, implementation, and deployment of a real-time feedback adaptive RMP ELM controller on the KSTAR tokamak. The controller has been designed to achieve two objectives. First, the controller must be able to reliably achieve ELM suppression. Second, the controller should be flexible enough to allow for the exploration of additional physics phenomena. In order to accomplish both these goals, the controller features multiple feedback modes, including several types of amplitude and phasing feedback. In addition, a so-called *adaptive lower bound* has been developed to allow the feedback controller to set and adjust minimum bounds on the applied RMP in real-time during the discharge. During experiments, this controller successfully optimized the applied RMP in real-time. Furthermore, the controller also achieved and sustained ELM suppression in a long pulse discharge for the first time.

Dedicated analysis on a single discharge of the feedback adaptive RMP ELM controller experiments is presented in the related—more physics focused—work by Kim *et al.*[40] Here, it is shown that the considerable recovery of confinement is not solely attributable to the feedback adaptive ELM controller action in a direct sense. Instead, there seems to be a contribution from an RMP-induced ion pedestal broadening, which promotes confinement recovery by improving the ion pedestal response and peeling-ballooning mode stability. In addition, a correlation between the pedestal widening and anomalous transport is presented. Such an interesting discovery was made possible by feedback 3D-field modulation via the ELM controller. This further supports the importance of developing a feedback adaptive RMP ELM controller as a means to investigate RMP physics mechanisms and optimize ELM control in future tokamaks. The work presented in this article will elucidate the fundamentals of such an adaptive scheme, focusing on the control design and the high-level results.

This paper is organized as follows: Since the capabilities of each fusion device are unique, the KSTAR real-time ELM control capabilities are outlined in Sec. II. The real-time ELM detector that is used as part of the ELM controller is detailed in Sec. III. In Sec. IV, it is described how these specific real-time control capabilities are leveraged to arrive at the feedback ELM controller design. Experiments are then conducted on the KSTAR tokamak to assess the ELM control performance of the controller and to use these novel capabilities to investigate several interesting physics phenomena, as discussed in Sec. V. Finally, conclusions from this study and a set of improvements that have been made to the algorithm since experimental implementation will be mentioned in Sec. VI.

II. KSTAR REAL-TIME ELM CONTROL CAPABILITIES

In this section, we describe in depth the real-time ELM controller developed for the KSTAR plasma control system (PCS). The PCS is a strict real-time system with high-speed computers that utilize high frequency, real-time data acquisition tools, and a deterministic real-time network supported by a real-time operating system. KSTAR's PCS consists of six central processing units (CPUs) (see Ref. 41 for further details). As such, the ELM controller developed in this work was implemented on a real-time CPU that runs at a fast cycle time sufficient for ELM control. Furthermore, controller operation requires that real-time diagnostic data are provided in a timely fashion and actuator signals are communicated sufficiently fast. As such, for the experiments discussed in this work, the KSTAR CPU1 is chosen with a 20 kHz cycle frequency to meet these demands.

A. Control sensors for ELM measurement

An essential part of the ELM controller is the plasma sensor, which must be able to sense all ELM behavior that might pose a threat to the device. To satisfy this constraint, the data sampling rate of the

sensor must be greater than the frequency of ELMs. At the time of implementation, only a single photo-diode was available for real-time use in the PCS, which fortunately meets this requirement. For this study, the primary plasma sensor is a poloidal photo-diode that measures D_α emission at a sampling rate of 20 kHz. For details about the general setup, the reader is referred to Ref. 42. We note, however, that the current system has been upgraded with respect to details in this previous publication. The current setup is depicted in Fig. 1, which shows the relevant photo-diode located around the outboard mid-plane with the divertor in its line of sight. This photo-diode detects deuterium Balmer alpha (D_α) line emission, providing a tangible measure of ELM events, which create a marked increase in D_α emission in the plasma edge. A Tee-ed raw voltage signal of the D_α emission measurement is provided to the PCS so that a real-time signal can be accessed in addition to the potential for offline analysis with minimal signal processing.

B. Control actuators

In order to be able to accurately apply a specific 3D resonant per-turbation, it is generally beneficial to have many available coils distrib-uted both poloidally and toroidally across the machine. The KSTAR tokamak hosts 12 in-vessel correction coils (IVCCs) with three rows of four toroidally distributed coils (outboard), as depicted in Fig. 2,
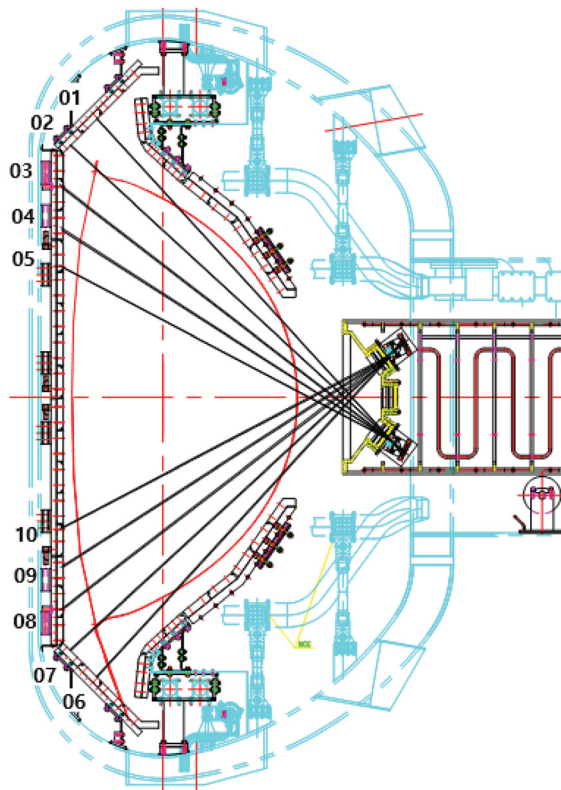

FIG. 1. Visible spectroscopy at KSTAR. The layout of the set of poloidal channels is represented by the photo-diode number and black lines of sight. The second poloidal (02) photo-diode is used by the ELM controller in this work.
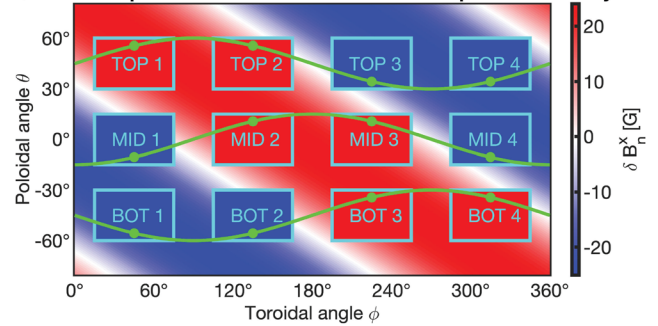

FIG. 2. The KSTAR IVCC set consists of three rows of four coils. In this particular pedagogical example, an $n = 1$ RMP is applied (as indicated by the green sinusoi-dal curves) in the top row. This $n = 1$ perturbation is generated by requesting (iden-tical) positive currents (red fill) for coils TOP 1 and TOP 2, while requesting (identical) negative currents for coils TOP 3 and TOP 4 (blue fill). In this setup, both phasings are set to 90°, as exemplified by the phase shifts in the green curves and the shifts in which coil is red vs blue. The spectrum of the magnetic perturbation that emerges from the combined effect of all 12 coils is indicated by the red/blue background contours.

(the reader is referred to Refs. 43 and 44 for further details regarding the IVCC system). By sending individual current requests to all 12 coils, the range and accuracy of the applied magnetic perturbations spectra can be maximized. Therefore, all 12 IVCCs are included as actuators for the ELM controller. Specifically, the controller back-end is designed to work with KSTAR's STD-N1H patch panel, which requires current requests associated with the middle row of coils in the form

$$I_{\mathrm{MID,REQ}} = I_{\mathrm{MID}} \sin(\theta_{\mathrm{MID}}), \tag{1}$$

where I_{MID} is the amplitude and θ_{MID} is the phase of the middle coil set. From asymmetry, only the relative phases *between* the rows should affect ELM suppression and not the absolute phases themselves.[45] Therefore, the phases of the top (θ_{UP}) and bottom (θ_{BOT}) rows of coils are related to the phase of the middle row of coils through their respec-tive phasings ϕ_{TM} and ϕ_{MB}

$$\phi_{\mathrm{TM}} = \theta_{\mathrm{MID}} - \theta_{\mathrm{UP}}, \tag{2}$$

$$\phi_{\mathrm{MB}} = \theta_{\mathrm{BOT}} - \theta_{\mathrm{MID}}. \tag{3}$$

The current requests for the top and bottom rows of coils then consist of their respective amplitude (I_{UP} or I_{BOT}) multiplied by a trigonomet-ric function applied to θ_{UP} or θ_{BOT}. Details regarding which trigono-metric functions are used to generate the desired spectra can be found in Sec. IV D 2. This selection of trigonometric functions enables the controller to apply an $n = 1$ perturbation—a sinusoidal spectrum in the toroidal sense, where only a single period fits within the toroidal circumference, as opposed to two periods in the case of $n = 2$.

To demonstrate the operating space for RMP ELM suppression with respect to phasing, an example configuration modeled with the IPEC-code (which is explained in more depth in Sec. V) is presented in Fig. 3. In this polar plot, the radial coordinate represents the RMP amplitude, whereas the angular coordinate represents the RMP phas-ing. It can be seen that both the amplitude and phasing control are important in optimizing the path the ELM controller takes through
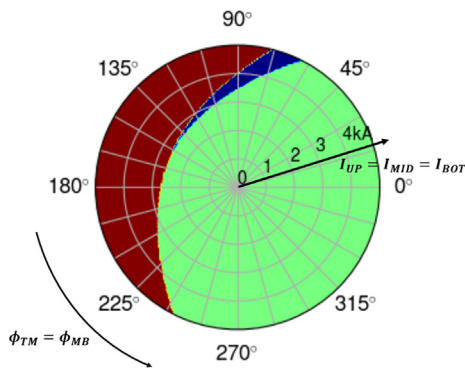
FIG. 3. 3D coil phase space ($I_{UP} = I_{MID} = I_{BOT}$, $\phi_{TM} = \phi_{MB}$) for an $n = 1$ resonant field on KSTAR is predicted by IPEC. Blue, red, and green regions in the polar plot represent spaces with ELM suppression, disruptions driven by locked modes, and sub-critical RMP resonance, respectively. The phasings are in degrees and the amplitudes in kA/turn.

statespace to minimize the applied RMP while remaining in an ELM suppressed regime, which is denoted by the blue shaded regions. To maximize the flexibility of the controller, it is, therefore, prudent to design the controller with the capability to determine I_{UP}, I_{MID}, I_{BOT}, ϕ_{TM}, and ϕ_{MB} in feedback, while θ_{MID} can be treated as a feed-forward signal.

C. Outline of the complete control loop

With these sensors and actuators, the complete control loop can be constructed as follows: The photo-diode measures D_α radiation in real-time and sends the signal to the PCS. The D_α-signal is fed into the real-time ELM detector, which tracks the ELM behavior and sends this information to the ELM controller. Depending on the mode of operation of the controller, it will use the information from the ELM detector to inform current requests that it sends to the power supplies of all 12 IVCCs. The 3D magnetic perturbations generated by the IVCCs should affect the ELM behavior of the plasma as desired. This completes the loop, which is also schematically represented in Fig. 4.

III. DESCRIPTION OF THE REAL-TIME ELM DETECTOR

A compact description of the real-time ELM detector is provided in this section for convenience; more information can be found in Ref. 46. As described above, D_α measurements provided by the photo-

diode serve as the input signal for the real-time ELM detector, which tracks both frequency and size of ELM events. A schematic representation of the components of the ELM detector is presented in Fig. 5.

A. ELM detection mechanism

To aid in the detection of ELM events, several modifications are applied to the raw D_α signal within the ELM detection algorithm. First, the D_α signal is passed through an RC low-pass filter to obtain a smoothed signal (S-signal). In parallel to the RC low-pass filter, the derivative of the D_α signal is determined. This derivative signal serves as an input to two additional filters, denoted by SD_1 and SD_2. Then, if $(D_\alpha - S)$, $|SD_1|$, or $|SD_2|$ exceed a specific threshold, the detector will classify this time slice as part of an ELM cycle. By default, the ELM detector will output zeros if no ELM behavior is currently being detected [see Fig. 5(b), in black]. During detected ELM cycles, the detector will output ones. This detection signal is sent through a low-pass filter once more to obtain a signal that can be loosely interpreted as a normalized ELM frequency (hereafter referred to simply as f_{ELM} or "ELM frequency"), where the absence of ELM behavior results in an ELM frequency that tends to zero, as opposed to tending to unity when ELM behavior is detected continuously [see Fig. 5(b), in blue].

IV. CONTROLLER DESIGN

By design, the feedback adaptive RMP ELM controller has complete control over the current requests that are sent to the RMP coil power supplies. To determine appropriate $n = 1$ perturbations, the controller always outputs five power supply commands, as described above. This is executed in a patch-panel configuration where the RMP associated with the middle row of coils is an $n = 1$ non-rotating standing wave (up to 5 kA), while the top and bottom rows generate a rotating waveform with a certain phasing with respect to the middle row. As such, in order for the ELM controller to be able to generate the desired RMP spectrum, it needs to assign both the amplitudes and phases of the current requests for each of the rows of coils separately.

A. Controller objectives and design perspectives

The primary objective of the feedback adaptive RMP ELM controller is to obtain complete control over the ELM frequency. In addition, we specify two additional design constraints:

First, it should become a tool that can be used to reliably achieve feedback controlled ELM suppression with minimal impact on
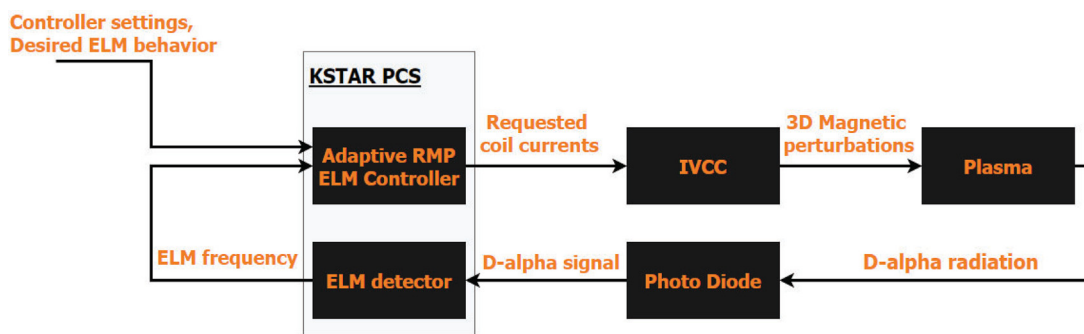
FIG. 4. This simplified diagram shows the main feedback control loop used by the feedback adaptive RMP ELM controller.
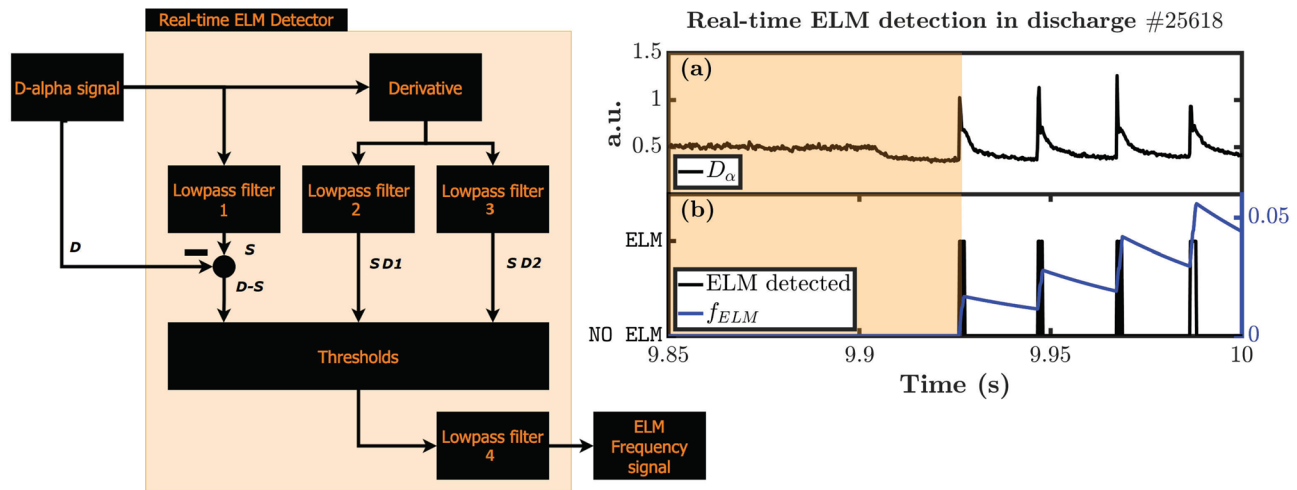
FIG. 5. Schematic representation of the inner workings of the real-time ELM detector (left) and an example of ELM detection (right). Panel (a) shows the D_α-trace, and panel (b) shows the raw ELM detection in black and the derived ELM frequency in blue.

performance parameters. To accommodate this, the controller should be able to minimize the amplitude of the applied RMP once ELM suppression has already been achieved. Since the minimum required RMP amplitude is not known *a priori*, the controller must be able to adaptively apply a lower bound on the applied RMP, so as to not lose ELM suppression once it has been obtained.

Second, the ELM controller should serve to advance our understanding of RMP ELM suppression physics (like hysteresis effects, turbulence, etc.). Therefore, the operator should have significant freedom in altering the specific waveforms generated by the controller. For example, in addition to amplitude feedback, it would also be interesting to explore optimization of the coil phasing, which requires the controller to include modes of operation where phasing feedback can be applied while using feed-forward amplitudes. To achieve this objective, the controller is, thus, designed to have multiple modes of operation and flexible parameters that can be set independently through the PCS.

B. Controller structure

To meet these objectives, several distinct *control types* have been developed for routine use. In all scenarios, the controller must provide six quantities that define all the coil currents: the current amplitudes for each row I_{UP}, I_{MID}, and I_{BOT} and the associated current phases θ_{UP}, θ_{MID}, and θ_{BOT}. In the KSTAR PCS, feed-forward waveforms for the amplitude are $I_{UP,FF}$, $I_{MID,FF}$, and $I_{BOT,FF}$. The feed-forward waveform for the phase of the middle row of coils is denoted by $\theta_{MID,FF}$, and the phases of the bottom and top row are determined by the feed-forward waveforms for the phasings $\phi_{TM,FF}$ and $\phi_{MB,FF}$. A simplified overview of the main *control types* and modes of operation of the controller is provided in Fig. 6.

In addition to the standard *control type* where only feed-forward waveforms are used (*control type* FF only), there are two main feedback *control types* available for selection. *Control type* FF + amplitude feedback includes modes of operation where coil current amplitude requests can be determined in feedback, while the controller uses feed-

forward waveforms for the phases. Conversely, *control type* FF + phasing feedback includes modes of operation where coil current phasing requests can be determined in feedback, while the controller uses feed-forward waveforms for the amplitudes. For each of these *control types*, the user still has freedom to choose a specific mode of operation within the *control type*. Finally, the *control type* full feedback can be selected if the objective is to apply feedback to both current amplitude and phasing requests.

A more in-depth description of each *control type* is presented next

1. FF + amplitude feedback

If this *control type* is selected, the user is asked to specify which coils will be controlled in feedback. By selecting I_UP only, I_MID only, or I_BOT only, the controller will only affect the amplitude of the current request of the respective row, while simultaneously using feed-forward waveforms for the amplitude of current requests of the other two rows. The only way to apply amplitude feedback on all three rows of coils simultaneously is by selecting the mode I_UP ratio. Here, the amplitudes of the middle and bottom rows are taken as a ratio with respect to the value of the top row, which itself is determined in feedback.

2. FF + phasing feedback

The FF + phasing feedback *control type* has three phasing feedback modes. Phasing feedback mode phi_TM only can be used for phasing feedback control of ϕ_{TM}. The other phasing (ϕ_{MB}) is then determined by feed-forward waveforms, as are the current amplitudes. Analogously, phasing feedback mode phi_MB only can be used for phasing feedback control of ϕ_{MB}. To control both phasings in feedback, the user may select the *control type* phi_TM and phi_MB.

C. The feedback calculation mechanism

It is not uncommon in feed-forward RMP ELM suppression experiments to apply RMPs in a step-like fashion. However, as the
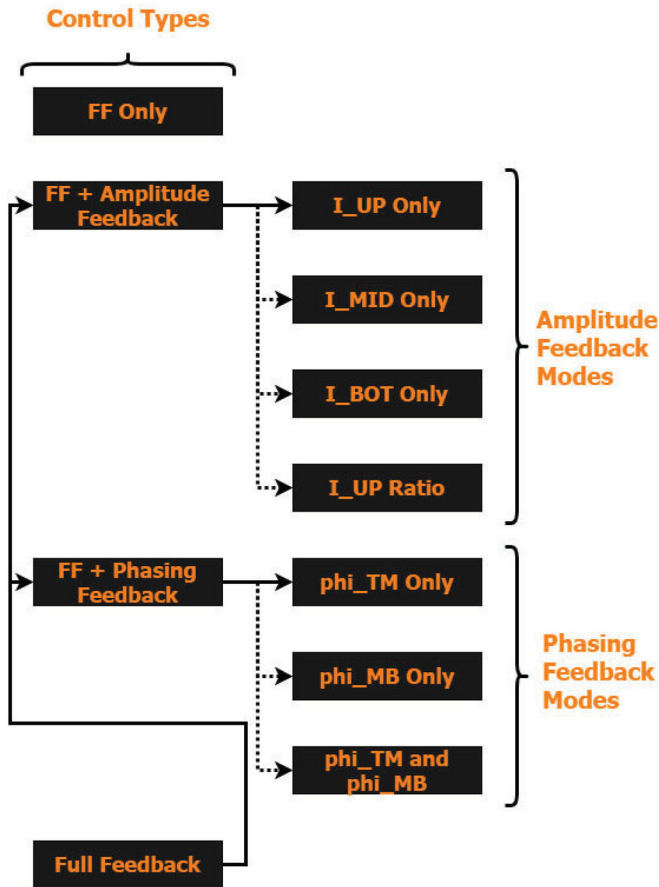
FIG. 6. The left vertical column of options represents the various available *control types.* The controller can be used to do feed-forward only (FF only), feed-forward with amplitude feedback (FF + amplitude feedback, keeping phasings feed-forward), feed-forward plus phasing feedback (FF + phasing feedback, keeping amplitudes feed-forward), and full feedback, where both the amplitudes and phasings are determined in feedback. The right vertical column represents the *feedback control modes* that can be used within a certain *control type.*

objectives of the feedback ELM controller developed in this work are not only to achieve ELM suppression but also to facilitate physics experiments, more flexibility in the shape of the RMP request is required.

To achieve ELM suppression with amplitude feedback control, the RMP amplitude is increased at a constant rate, which can be chosen by the operator. Then, once ELM suppression is obtained, the controller will hold the signal constant for a pre-determined time (user input), which can also be set to zero. During this ELM suppressed phase, it may be desirable to minimize the applied RMP amplitude in order to improve plasma performance. To do so, a linear ramp down rate may be specified. During ramp down, however, the operator may also select the ramp down *amplitude decrement* in addition to the slope. After the controller has decreased the requested RMP amplitude by the prescribed decrement, the controller holds the signal constant for a pre-determined time (user input), which can also be set to zero.

The situation is slightly different when operating with phasing feedback control, which is designed to explore whether the controller can achieve and sustain ELM suppression while optimizing for plasma performance or stability. In the first implementation, the phasing can be increased linearly at a user defined slope until ELM suppression is achieved. If the slope is chosen to be negative, the phasing will be decreased until ELM suppression is achieved. Once again, the controller can hold the phasing steady for a pre-determined amount of time once ELM suppression is achieved. Then, the phasing can be decreased incrementally (with pre-determined steady times) to find the optimal phasing.

1. Feedback calculation implementation

The similarities between the desired features of the feedback calculations for amplitude feedback and phasing feedback facilitate the development of a single feedback calculation mechanism, as presented in Fig. 7. This mechanism is comprised of a *finite state machine* (FSM) with three *states*: RAMPUP, FLAT, and RAMPDOWN. Here, we use K_k to denote the output of the feedback calculation mechanism, where the subscript k represents the PCS cycle. The calculations within each *state* and the conditions for changing *states* are outlined below.

a. The RAMPUP state. While in the RAMPUP state, the output K_k is updated once every PCS cycle according to

$$K_k = K_{k-1} + \Delta t_k R_{\mathrm{rampup,k}}, \tag{4}$$

where K_{k-1} represents the value of the output of the previous PCS cycle, Δt_k is the time elapsed between the current and previous PCS cycle, and $R_{\mathrm{rampup,k}}$ is the value of the feed-forward waveform of the desired slope associated with the current PCS cycle. During each PCS cycle, the algorithm checks the ELM detector output to determine whether or not ELM suppression has been achieved. If ELM suppression has been achieved, the feedback calculation moves to the FLAT *state* before executing the calculations of the next PCS cycle. If ELM suppression is **not** achieved, the *state* will not change.

b. The FLAT state. The length of time the controller will remain in the FLAT state is described by the parameter $T_{timer,k}$, which can be set separately for the two cases where the FLAT state is entered after either the RAMPUP or RAMPDOWN states. Since the output variable is kept steady while in the FLAT state, we have

$$K_k = K_{k-1}. \tag{5}$$

During each PCS cycle, the time left in the FLAT *state* is updated

$$T_{\mathrm{timer,k}} = T_{\mathrm{timer,k-1}} - \Delta t_k. \tag{6}$$

As long as $T_{\mathrm{timer,k}} > 0$, the FLAT *state* remains active. However, if the timer has run out, the controller checks the ELM detector to determine whether or not ELMs are suppressed. If the ELMs are **not** suppressed, the next *state* will be the RAMPUP *state*. On the other hand, if ELMs are still suppressed, the mechanism moves to the RAMPDOWN *state*.

c. The RAMPDOWN state. If the RAMPDOWN state is entered after the FLAT state, the total output decrement is initialized

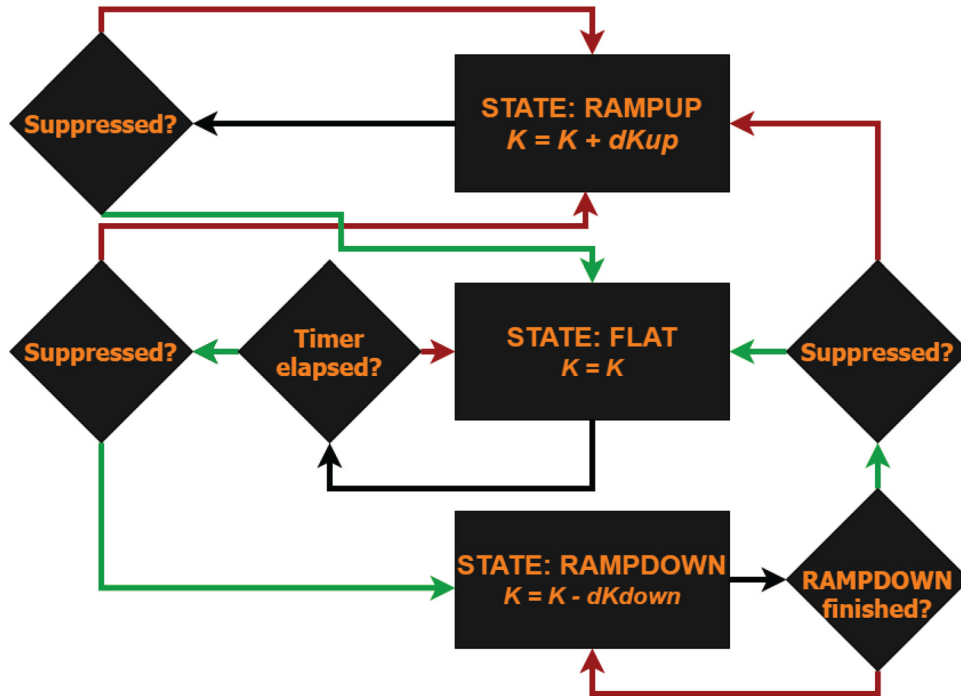$$\Delta K_{\mathrm{left,k}} = \Delta K_{\mathrm{rampdown,k}}, \tag{7}$$

FIG. 7. A simplified diagram of the finite state machine based feedback calculation mechanism used by the feedback adaptive RMP ELM controller for both amplitude and phasing *feedback control modes*. The *states* are represented by black rectangles, while the guard conditions for switching between *states* are represented by black diamonds. The green arrows indicate paths taken when the guard conditions are met, while red arrows indicate paths taken while guard conditions are not met (yet).

where $\Delta K_{\text{left,k}}$ is the total output decrement, which is set equal to the feed-forward waveform that denotes the desired (incremental) reduction of the output variable. After initialization, the output variable is updated

$$K_k = K_{k-1} - \Delta t_k R_{\text{rampdown,k}}, \tag{8}$$

where $R_{\text{rampdown,k}}$ is the desired variable ramp rate. For each PCS cycle in the RAMPDOWN *state*, the controller checks if the change in the output variable by $\Delta K_{\text{left,k}}$ has been accomplished or if the slope associated with ramping down is set to zero. If not, a required residual reduction

$$\Delta K_{\text{left,k}} = \Delta K_{\text{left,k-1}} - \Delta t_k R_{\text{rampdown,k}} \tag{9}$$

is implemented. Alternatively, if these conditions are satisfied, the controller checks the ELM detector to determine whether ELMs are suppressed. If ELMs are not currently suppressed, then the next *state* will be the RAMPUP *state*. On the other hand, if ELMs are indeed suppressed, then the next *state* will be the FLAT *state*.

The intended behavior of the FSM-based feedback calculation mechanism is summarized in Fig. 8. In this example, $R_{\text{rampup}} = 1$. At $t = 2$ s, the first instance of ELM suppression is detected. The controller then moves from the RAMPUP *state* to the FLAT *state* for a steady time of $T_{\text{steady,up}} = 1$ s. Since ELMs are still being suppressed after the steady time has elapsed, the controller moves to the RAMPDOWN *state*. After the ramp down decrement has been realized, the controller rechecks for ELM suppression and repeats this process. However, during the ramp between 5 and 6 s, ELM suppression is lost. Thus,

after finishing that ramp down decrement, the controller moves to the RAMPUP *state*.

2. Adaptive lower bound for confinement optimization

Using the design described above, the controller will repeatedly ramp down incrementally until loss of ELM suppression, before ramping up again. To prevent this pattern from happening indefinitely, an
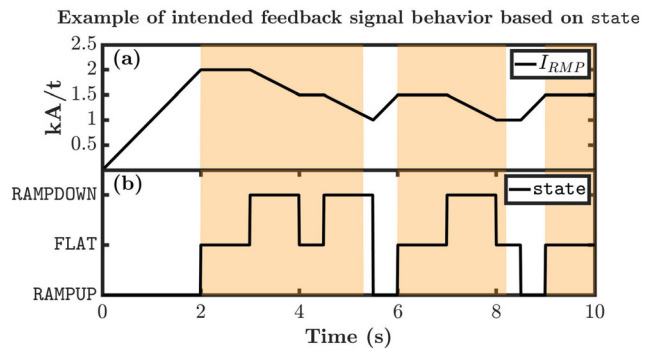

FIG. 8. An example of intended behavior of the feedback calculation showing the desired functionality of the adaptive ELM controller. The black curve in panel (a) represents the feedback RMP current amplitude that is computed based on the states shown in panel (b). The FSM switches states depending on the ELM activity. White areas indicate times during which ELMs are not suppressed.

optional *adaptive lower bound* feature has been developed. If the adaptive lower bound feature is selected, one can choose either to use a feed-forward waveform for the adaptive lower bound on the output variable or to let the controller determine the lower bound in feedback. The implementation of the adaptive lower bound is outlined as follows: When the controller is in the RAMPDOWN *state*, and it loses ELM suppression, it will store the value of the output at the moment of ELM suppression loss ($K_{loss} = K_k$). The controller will move to the RAMPUP *state* as usual. However, from this moment onward, if the controller enters the RAMPDOWN *state* again, the controller will not ramp down the output variable below a threshold

$$K_k \geq K_{LB,k}, \tag{10}$$

which is determined by

$$K_{LB,k} = K_{loss} + \Delta K_{LB,k}, \tag{11}$$

where $\Delta K_{LB,k}$ is a feed-forward waveform that denotes the desired increase in the adaptive lower bound each time ELM suppression is lost in the RAMPDOWN *state*.

D. Computation of RMP requests

As mentioned above, the feedback ELM controller has complete control over all five power supply commands for RMP current requests. A schematic representation of the required computations during each PCS cycle will be outlined below.

1. Computing the total amplitudes and phases

The total requested RMP current amplitudes for the top, middle, and bottom rows of coils are computed by summing their feed-forward and feedback contributions

$$I_{UP} = I_{UP,FF} + I_{UP,FB}, \tag{12}$$
$$I_{MID} = I_{MID,FF} + I_{MID,FB}, \tag{13}$$
$$I_{BOT} = I_{BOT,FF} + I_{BOT,FB}. \tag{14}$$

In order to be able to determine the phases, first the two total phasings are computed

$$\phi_{TM} = \phi_{TM,FF} + \phi_{TM,FB}, \tag{15}$$
$$\phi_{MB} = \phi_{MB,FF} + \phi_{MB,FB}. \tag{16}$$

The phases are now fully determined

$$\theta_{MID} = \theta_{MID,FF}, \tag{17}$$
$$\theta_{UP} = \theta_{MID} - \phi_{TM}, \tag{18}$$
$$\theta_{BOT} = \theta_{MID} + \phi_{MB}. \tag{19}$$

2. Generating the power supply RMP current requests

The total RMP amplitude and phase requests are used to compute the total RMP current requests as follows:

$$I_{IPS1,req} = I_{UP} \cos(\theta_{UP}), \tag{20}$$
$$I_{IPS2,req} = -I_{BOT} \cos(\theta_{BOT}), \tag{21}$$
$$I_{IPS3,req} = I_{BOT} \sin(\theta_{BOT}), \tag{22}$$

$$I_{IPS4,req} = -I_{UP} \sin(\theta_{UP}), \tag{23}$$
$$I_{IPS5,req} = \frac{1}{\sqrt{2}} I_{MID} \sin(\theta_{MID}). \tag{24}$$

V. EXPERIMENTAL RESULTS

In addition to validating the controller implementation, experiments were conducted on the KSTAR tokamak with the goals of (a) achieving and sustaining ELM suppression while minimizing the amplitude of the applied perturbations and (b) demonstrating the ability of the ELM controller to sustain ELM suppression throughout a long pulse (16 s) discharge. The details of these experiments are described below.

A. Suppression window and hysteresis

The reference discharge for the first feedback adaptive RMP ELM control experiments is depicted in Fig. 9. The main plasma parameters for this discharge are $B_T = 1.8$ T, $I_p = 0.52$ MA, elongation $\kappa \sim 1.72$, upper triangularity $\delta_{up} \sim 0.38$, lower triangularity $\delta_{low} \sim 0.87$, edge safety factor $q_{95} \sim 5.1$, neutral beam power $P_{NBI} \sim 3.1$ MW, and $\beta_N \sim 2.05$. Before RMP application, the pedestal density and temperature amounted to $n_{ped} \sim 2.25 \times 10^{19}$ m^{-3} and $T_{ped} \sim 0.85$ keV, respectively.

Before applying the controller, RMP was applied manually to determine the suppression window. As depicted in Fig. 9, ELM suppression was achieved at $t = 8.567$ s at an RMP amplitude of 2.14 kA/t and then lost at $t = 10.240$ s at an amplitude of 3.10 kA/t when the plasma is terminated due to locked modes. As such, the suppression window achieved in the reference discharge is approximately 1 kA/t, which is suitably large for the implementation of the controller.

Using the information obtained from reference discharge No. 25607, a feed-forward RMP is then applied to identify the hysteresis window. The applied RMP is increased linearly to a value high
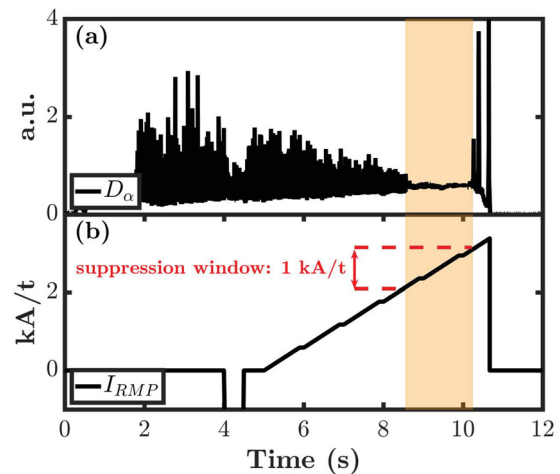
FIG. 9. Identifying the suppression window in the reference discharge: Panel (a) displays the D_α trace in black. Panel (b) shows the applied RMP in kA/t (black). The RMP is ramped linearly until the discharge disrupts due to locked modes. The suppressed period is shaded in orange. The suppression window amounts to approximately 1 kA/t.

enough to ensure ELM suppression (2.7 kA/t) then held steady for 1 s before a linear ramp down is initiated, as shown in Fig. 10. ELM suppression is achieved at $t = 7.421$ s at an RMP amplitude of 2.18 kA/t and lost at $t = 9.758$ s at an amplitude of 1.68 kA/t. As can be seen in Fig. 9, the hysteresis window observed in this discharge amounts to approximately 0.5 kA/t. The existence of this hysteresis window will be exploited in later discharges to recover performance during experiments with feedback minimization of the RMP.

B. First feedback controlled ELM suppression without ramp down

As a first demonstration, the controller is used simply to achieve and sustain ELM suppression in Fig. 11. To do this, the amplitude feedback mode is set to I_UP ratio with the amplitude of each coil row set to the same values, and the ramp down decrement is set to zero. The middle coils have phase $\theta_{MID} = 45°$, and the phasing offsets for the other two rows are set to $\phi_{TM} = \phi_{MB} = 90°$. As long as ELMs are not suppressed, the applied RMP will be increased until it reaches the maximum allowed RMP request, at which point it would hold steady at the limit.

In this discharge, the controller is turned on at $t = 5.000$ s. However, the ELM detector incorrectly detected ELM suppression due to transient behavior of the low-pass filter during initialization, delaying ramp up until $t = 5.200$ s. ELM suppression is then achieved at $t = 5.836$ s with an applied RMP of 2.44 kA/t, prompting the controller to move from RAMPUP to FLAT. As shown in panel (d), whenever the steady time has elapsed and the plasma is still ELM suppressed, the controller attempts to ramp down the RMP by moving to the RAMPDOWN *state*. However, since the ramp down decrement is set to zero for this experiment, the controller immediately goes back to
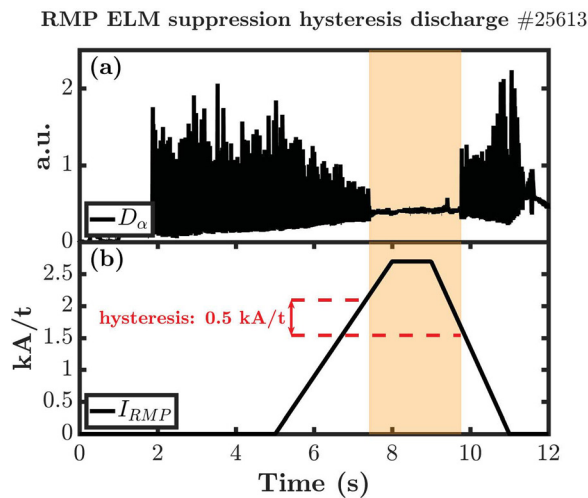

FIG. 10. Identifying and validating the hysteresis effect in the reference discharge: Panel (a) displays the D_α trace in black. Panel (b) shows the applied RMP in kA/t (black). The RMP is ramped linearly until ELM suppression is achieved. After some steady time, the RMP is linearly ramped down. The RMP current required to **enter** ELM suppression exceeds the RMP current required to **sustain** ELM suppression, since ELM suppression is lost at a lower amplitude than is needed to enter it. The suppressed period is shaded in orange. The observed hysteresis amounts to approximately 0.5 kA/t.
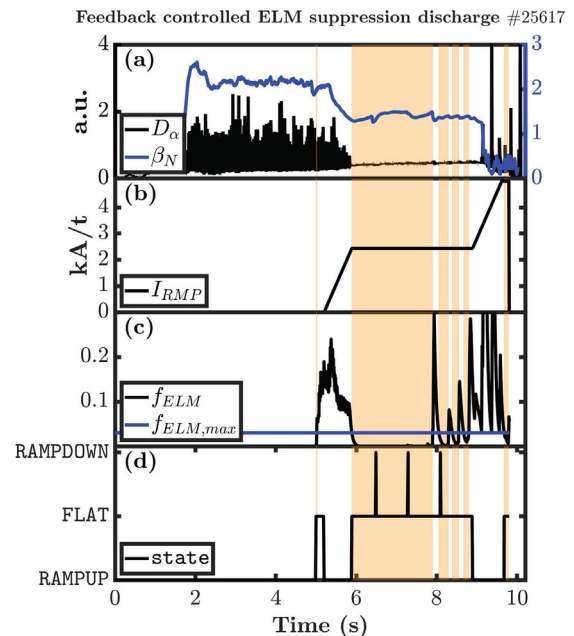

FIG. 11. Sustained ELM suppression is demonstrated on KSTAR using amplitude feedback. After the controller is turned on at $t = 5.000$ s, times where ELM suppression is detected are colored in orange. Panel (a) shows the D_α trace in black and β_N in blue. Panel (b) shows the applied RMP in black, and panel (c) depicts the calculated ELM frequency in black as well as the maximum allowed ELM frequency in blue. In this particular case, the ramp down decrement is zero. Panel (d) shows the controller *state*.

the FLAT *state* until ELM suppression is eventually lost at the end of the discharge.

During the ELM suppressed phase of this discharge, there are short intervals where the un-optimized ELM detector incorrectly detects a loss of ELM suppression. However, this does not change the controller state since, by design, the controller only evaluates ELM suppression after a steady time has elapsed, and not *during* any of those intervals. Eventually, the ELM detector incorrectly detects loss of ELM suppression during a cycle when the steady time in FLAT has elapsed and the controller moves to RAMPUP, leading to an actual loss of ELM suppression at an applied RMP of 3.30 kA/t. This observation is consistent with the suppression window obtained during the reference discharge (No. 25607), where ELM suppression was lost at approximately 3.10 kA/t. It is noteworthy that the normalized pressure (β_N) as indicated by the blue curve in panel (a) does not recover from the RMP induced degradation if the RMP is kept steady during ELM suppression. To recover performance, the applied RMP needs to be minimized.

C. First feedback controlled ELM suppression with ramp down

After demonstrating the capability of the controller to achieve and sustain ELM suppression in feedback, the next step is to use the RAMPDOWN capability in amplitude feedback mode I_UP Ratio to exploit the hysteresis effect and minimize the applied RMP. Using similar controller settings to those used in No. 25617, but with a ramp

down decrement set to 0.22 kA/t, the RMP strength is decreased in steps of length $\Delta t_{steady,down}$ after ELM suppression is achieved. As shown in Fig. 12, ELM suppression is retained at reduced RMP strength until around ~10 s, at which point suppression is lost.

As above, the ELM detector suffered from initialization effects and sub-optimally tuned parameters, causing an initial false positive ELM suppression detection and resulting in a short delay before the RMP is ramped up. In addition, the ELM detector incorrectly detects ELM suppression for a short period during the RMP ramp up, causing the controller to think it achieved ELM suppression and move to the FLAT *state*. After $\Delta t_{steady,up}$ has elapsed, however, the ELM detector correctly determines ELM suppression is not yet achieved, and then resumes ramping until ELM suppression is actually achieved at $t = 6.789$ s with an applied RMP of 2.78 kA/t. The controller successfully incrementally ramps down the RMP until ELM suppression is lost at $t = 9.927$ s with an applied RMP of 1.50 kA/t, at which point the process is restarted. An important observation in this experiment is that the RMP amplitude required to enter ELM suppression the **second** time (1.94 kA/t) is significantly lower than the amplitude that is initially required. Additionally, the RMP amplitude at which ELM suppression is lost the second time is greater than the amplitude at which ELM suppression is lost initially. This suggests that it might be possible to find a converged, optimized RMP amplitude using feedback in real-time.

From these demonstrations, it can be concluded that the feedback ELM controller works as intended and proves to be a useful tool to

FIG. 12. RMP amplitude may be decreased after ELM suppression has been achieved. Panel (a) shows the D_α trace in black and β_N in blue. Panel (b) shows the applied RMP in black. Panel (c) depicts the calculated ELM frequency in black and the maximum allowed ELM frequency in blue (below which the discharge is considered ELM suppressed). Panel (d) shows the controller *state*. Times during which ELM suppression is detected are colored in orange.

achieve, sustain, and optimize ELM suppression. However, it was also evident that the ELM detector needed to be tuned to remove any false detection results causing the controller to lose ELM suppression.

D. Confinement optimization using the adaptive lower bound

An example of feedback ELM suppression using amplitude feedback and the adaptive lower bound feature is shown in Fig. 13. This experiment was conducted in a plasma with $R_0 = 1.8$, $a_0 = 0.45$ m, $B_T = 1.8$T, $n_G \sim 0.4$, $\kappa \sim 1.71$, $\delta_{up} \sim 0.37$, $\delta_{low} \sim 0.85$, and pedestal collisionality $\nu_{e,ped} \sim 0.5$. The feedback ELM controller is set to detect only between $t = 0$ and $t = 5.300$ s in order to avoid potential transient effects from low-pass filters once it is set to control. In addition, the ELM detector was re-tuned prior to this experiment.

As seen in Fig. 13, the controller begins operation at $t = 5.300$ s when it starts to linearly increase the requested RMP until it achieves ELM suppression at 6.622 s. Once ELM suppression has been achieved, the controller holds steady for a pre-determined time interval of 0.500 s. If the controller has sustained ELM suppression during this interval, it will start to linearly minimize the applied RMP.

To demonstrate the functionality of the adaptive lower bound, panel (d) of Fig. 13 displays the feedback initialized RMP minimization starting at 7.122 s. The controller keeps reducing the applied RMP current until the detector flags loss of ELM suppression at 7.713 s. At this point, the adaptive lower bound feature is triggered, as indicated by the blue curve in Fig. 13(d). The controller notes the RMP current at which suppression is lost, I_{loss}. It stores this lower bound, incremented by a safety margin $\Delta I_{LB,k}$, i.e., $I_{LB,k} = I_{loss} + \Delta I_{LB,k}$. For this particular discharge, $I_{loss} = 1.64$ and $\Delta I_{LB,k}$ was set to 0.070 7 kA/t. Now that the adaptive lower bound has been initiated, the controller starts ramping up the applied RMP to regain ELM suppression. ELM suppression is regained at 8.004 s. Again, the controller holds steady for the pre-determined amount of time before attempting to minimize the applied RMP. However now, the applied RMP can never drop below the adaptive lower bound set by the controller. In this discharge, it turned out the initial lower bound set by the controller was not sufficient yet to sustain ELM suppression indefinitely, as ELM suppression is lost for the second time at 8.758 s. The controller applies an updated adaptive lower bound and repeats the steps mentioned above. As shown by the red stars and diamonds and red dashed curves in panel (d), the RMP request converges throughout the shot. The RMP amplitude required to access ELM suppression the first time amounts to approximately 2.80 kA/t (using *detected* ELM suppression). However, when it enters the last ELM suppression phase of the discharge, only 1.94 kA/t is required—a reduction of the order of 30%.

The effects of this reduction in the required RMP strength can be visualized in Fig. 13(c), which displays β_N. By optimizing the applied RMP using feedback in real-time, the controller is achieve $\beta_{N,opt} = 1.9$ by the end of the optimization of ELM suppression, starting from $\beta_{N,init} = 1.4$ at the first visually detected ELM suppressed phase (compared to $\beta_{N,NO-RMP} = 2.2$ before RMP application). This translates to the controller regaining upwards of 60% of confinement, thereby minimizing the negative impact on performance while sustaining ELM suppression as much as possible, and no significant changes in the electron density at the pedestal are observed during RMP reduction.
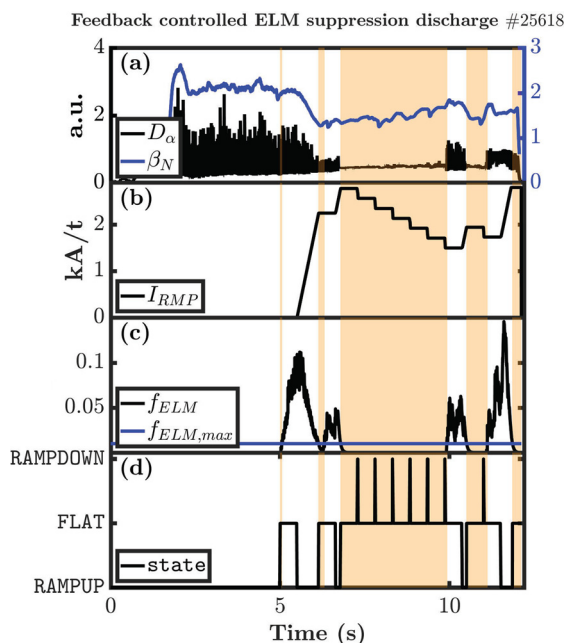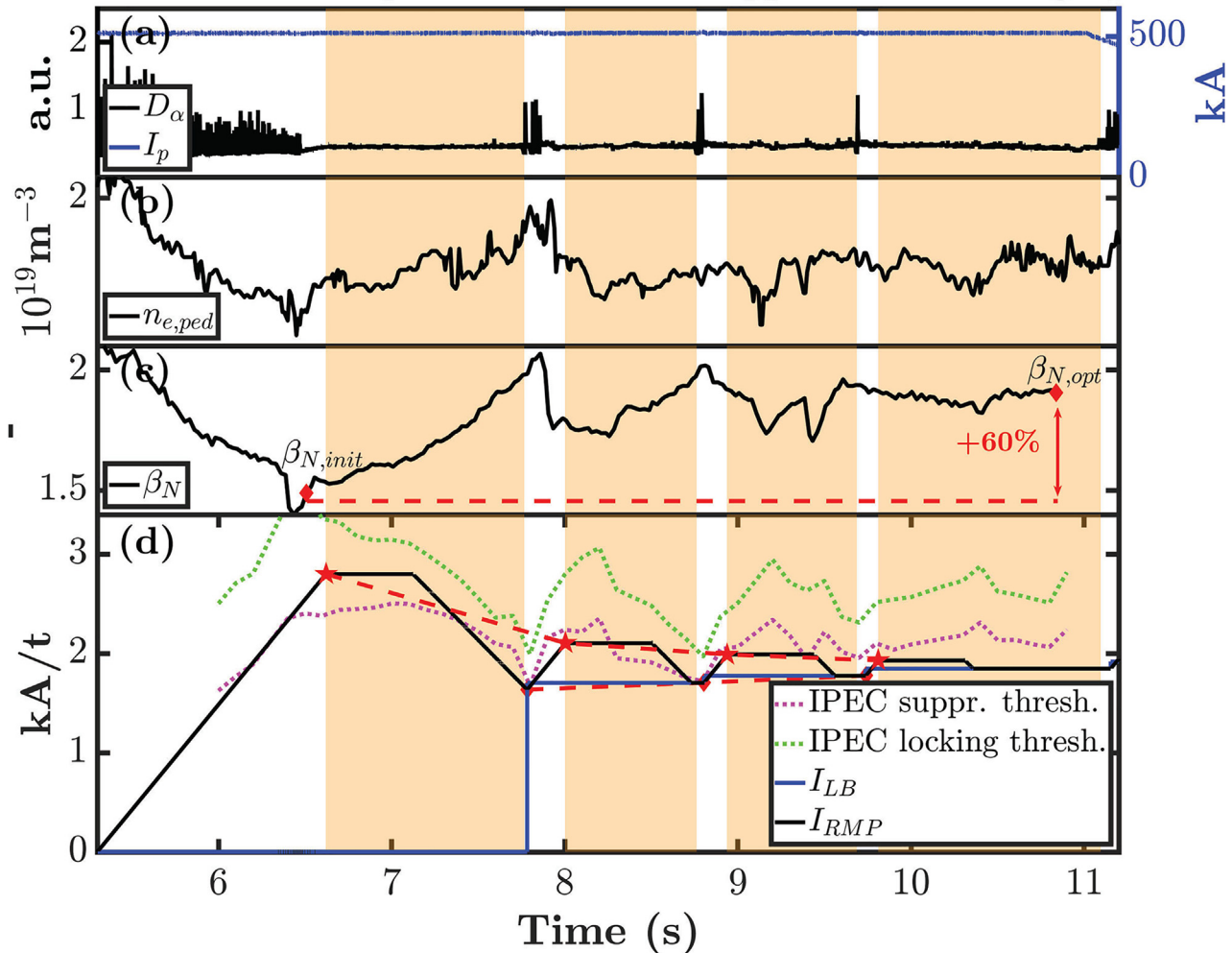
FIG. 13. Amplitude feedback controlled ELM suppression with performance optimization and adaptive lower bound: Panel (a) shows the D_α trace in black and the plasma current in blue. The shaded orange areas represent ELM suppression as detected by the ELM detector. Panel (b) shows the evolution of electron density as measured at the pedestal top in black. β_N is represented by the black curve in panel (c) with the red diamonds indicating the normalized pressure at the start of ELM suppression and end of ELM suppression. The applied RMP current is shown in black in panel (d). The blue curve shows the evolution of the adaptive lower bound. Importantly, the RMP required to sustain ELM suppression eventually converges, as demonstrated by the red stars (suppression entrance) and red diamonds (suppression exit) and red dashed curves. The magenta dotted curve and green dotted curve represent the predicted RMP threshold for ELM suppression and the locking thresholds from the IPEC-code.

E. Sustaining ELM suppression in long pulses

After successful application of the controller during a regular pulse, the controller was used in a long pulse discharge to evaluate whether it can sustain ELM suppression during long pulses as well, which is historically difficult on KSTAR. The results of the long pulse experiment are displayed in Fig. 14. For this discharge (No. 26013), the same main controller setup is used as in No. 26004.

The controller is activated at $t = 5.300$ s. The ramp up stops around $t = 7.170$ s, while the plasma is still exhibiting lower level ELM activity since the requested RMP current at this point was about to exceed the maximum allowed RMP request. This boundary on the

maximum RMP current request serves to prevent disruptions in cases where the controller would keep ramping up the currents beyond reasonable limits. Once the RMP request reaches the limit value, it is held steady at that level until the requested currents are below the threshold. To preserve the applied spectrum as much as possible, all coil currents are scaled with respect to each other, such that the ratio between the rows of coils remains unchanged.

Interestingly, the controller still achieves ELM suppression at $t = 7.660$ s, stressing the importance of choosing a sensible ramp up rate of the RMP. After $\Delta t_{steady,up}$ has elapsed, RMP minimization is initiated. Similar to No. 26004, $\Delta t_{steady,down}$ is set to zero in this case throughout the discharge. During its normal operation, the controller

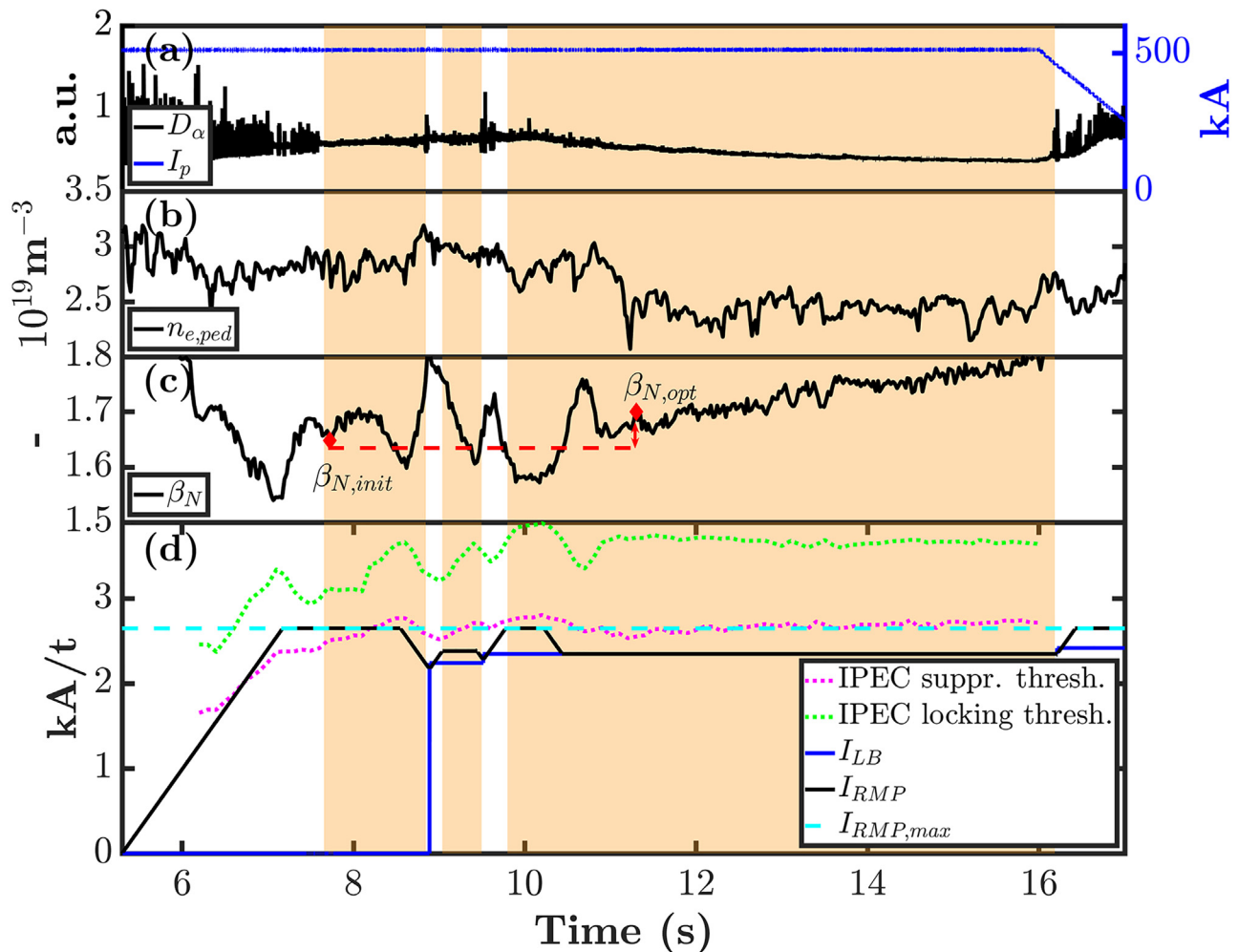## Feedback controlled long pulse ELM suppression discharge #26013

FIG. 14. Amplitude feedback controlled long pulse ELM suppression with adaptive lower bound: Panel (a) shows the D_α trace in black and the plasma current in blue. The shaded orange areas represent ELM suppression as detected by the ELM detector. Panel (b) shows the evolution of electron density as measured at the pedestal top in black. β_N is represented by the black curve in panel (c), with the red diamonds indicating the normalized pressure at the start of ELM suppression and after RMP amplitude optimization in this discharge. The applied RMP current is shown in black in panel (d). The blue curve represents the adaptive lower bound and the cyan dashed curve represents the maximum allowed RMP request. The magenta dotted curve and green dotted curve represent the predicted RMP threshold for ELM suppression and the locking thresholds from the IPEC-code.

loses ELM suppression two times, at $t = 8.840$ and $t = 9.470$ s, updating the adaptive lower bound each time. After 10 s into the discharge, the gas puff was reduced to zero, resulting in the dropping base level of the $n_{e,ped}$ and D_α traces. During the RMP minimization starting at $t = 9.440$ s, the requested RMP can eventually not be reduced any further due to the lower bound, so the applied RMP current remains constant. With this setting, the controller is able to sustain complete ELM suppression for 6.380 s, until the end of the discharge.

Another interesting observation regarding confinement recovery is well illustrated in Fig. 14. A boosted confinement recovery can be seen during the period where the RMP amplitude is held steady at the adaptive lower bound. The exact underlying mechanism is still a subject of active research and out of the scope of the work presented here. However it is noteworthy to mention at this time that, upon preliminary inspection of additional plasma discharges, there seems to be a correlation between the baseline level of the D_α signal and the boosted confinement recovery: when the baseline signal decreases, confinement is boosted. Since D_α is related to the various boundary parameters, including the edge neutral density, recycling, separatrix temperature, and density profile, we suspect that one of these parameters may play a considerable role here, and this will be included in future work.

Previous work has shown that the plasma enters ELM suppression once the perturbed radial field in the pedestal region ($\delta B_{r,edge}$) exceeds a certain threshold[45] while core-locking occurs with large core

perturbations ($\delta B_{r,core}$) above the locking-threshold. The IPEC code[47] is used to compute these field responses required for ELM suppression by averaging δB_r between $0.9 \leq \psi_N \leq 1$ and $0 \leq \psi_N \leq 0.9$, respectively. The thresholds of $\delta B_{r,edge} \sim 20$ G for ELM suppression and $\delta B_{r,core} \sim 35$ G for core-locking are obtained from the adjacent discharges. Based on these values, IPEC can be utilized to predict the required RMP amplitude for ELM suppression and locking threshold over time.

Figures 13 and 14 illustrate such predictions are well satisfied where the first ELM suppression is achieved when the RMP amplitude exceeds the derived thresholds. However, as time progresses in the discharge, the plasma changes in a way such that the predictions become less effective in guiding the RMP amplitude. This tendency becomes clearer in No. 26013 (magenta dotted curve), where the second ELM suppression is achieved below the predicted threshold at 9.500 s. Because ELM control will require accurate real-time predictors in the future, this stresses the importance of improved models, which can predict ELM suppression in later phases of discharges.

Notably, the adaptive control lowers the RMP strength after entering the ELM-free state and maintains it near the levels for marginally stable ELM suppression. This automatically avoids touching the disruptive limits. As shown in Figs. 13 and 14, the RMP strength stays safely below the disruption threshold (green dotted line) throughout the discharges, highlighting the advantages of this adaptive scheme for achieving safe and stable ELM suppression.

VI. CONCLUSIONS AND FUTURE WORK

The feedback adaptive RMP ELM controller developed in this work has proven to be capable of achieving and sustaining ELM suppression for significant portions of experimental discharges. In addition, it was shown that the controller can be used to minimize the applied RMP current during ELM suppression. A benefit of this minimization is that it will allow for longer discharges, since the flux consumption is reduced in line with the RMP strength. Furthermore, plasma performance itself is maximized as a result of the RMP minimization, as evidenced by the 60% increase in β_N between the first moment of ELM suppression and the last. Since ELM suppression was temporarily lost in the long pulse, the adaptive lower bound was set high, allowing for less minimization of the applied RMP current. As a result, the gain in performance is not as impressive as in No. 26004. However, the demonstration of sustained ELM suppression during most of the discharge shows the potential of this approach.

Overall, the controller worked as intended. However, the ELM detector suffered from a few false positive and false negative detections of ELM suppression, causing the controller to behave sub-optimally. Therefore, in the future work, the ELM detector should be replaced by a more robust ELM detector that does not rely on calibration-specific tuning. Furthermore, it is clear that the current controller design will inevitably need to lose ELM suppression before it can find the minimum required RMP current for ELM suppression. Since several of the KSTAR real-time diagnostics seem to exhibit precursors to the loss of ELM suppression, an ELM suppression-loss precursor-detector is being developed. By using the information from the real-time precursor detector, the controller might have sufficient time to adjust the 3D fields before the ELM materializes, thereby still preventing the excessive transient heat load to the divertor that would otherwise be caused by a transient loss of ELM suppression.

The phasing feedback control and full feedback control modes of the controller have not yet been demonstrated in experiments and will be the subject of future work. The controller will also be extended such that it can be used within the so-called STD-N1K and MXD-CMB patch panel setups, which will allow for rotating $n = 1$ RMP fields as well as $n = 2$ spectra, respectively. By extending the capabilities of the controller, we hope to determine the most effective way of achieving and sustaining ELM suppression, as well as being able to serve more physics experiments.

Even though the controller cannot yet be tested in true ITER conditions, no insoluble complications are foreseen for the applicability of a controller of this sort in an ITER-scale reactor. The deployment of this type of controller is, in principle, not scenario specific. Instead, it is crucial to have a plasma with an accessible ELM suppression window. In general, low q_{95} and edge collisionality are observed to be favorable for the existence of the ELM suppression window. So far, projections for the ITER scenarios originate from model-based predictions. So at least for the ITER-baseline scenarios (IBS), it seems like that this controller could prove effective. For instance, the theoretical and experimental studies by Hu et al.[48] and Fenstermacher et al.[49] predict the accessibility of ELM suppression in IBS. For other scenarios, though, as long as the suppression window exists, the controller can, in principle, be used. However, to gain more certainty about the applicability in those scenarios, more predictive work is needed, which may be outside of the scope of this work.

For a more in-depth publication on the physics insights gained during the experiments with the feedback RMP ELM controller, the reader is referred to Ref. 40.

AUTHOR DECLARATIONS
Conflict of Interest

The authors have no conflicts to disclose.

DATA AVAILABILITY

The data that support the findings of this study are available from the corresponding author upon reasonable request.

REFERENCES

[1] F. Wagner, G. Becker, K. Behringer, D. Campbell, A. Eberhagen, W. Engelhardt, G. Fussmann, O. Gehre, J. Gernhardt, G. v. Gierke, G. Haas, M. Huang, F. Karger, M. Keilhacker, O. Klüber, M. Kornherr, K. Lackner, G. Lisitano, G. G. Lister, H. M. Mayer, D. Meisel, E. R. Müller, H. Murmann, H. Niedermeyer, W. Poschenrieder, H. Rapp, H. Röhr, F. Schneider, G. Siller, E. Speth, A. Stäbler, K. H. Steuer, G. Venus, O. Vollmer, and Z. Yü, "Regime of improved confinement and high beta in neutral-beam-heated divertor discharges of the ASDEX tokamak," Phys. Rev. Lett. **49**, 1408–1412 (1982).

[2] T. E. Evans, "ELM mitigation techniques," in *Proceedings of the 20th International Conference on Plasma-Surface Interactions in Controlled Fusion Devices, 2012* [J. Nucl. Mater. **438**, S11–S18 (2013)].

[3] A. W. Leonard, "Edge-localized-modes in tokamaks," Phys. Plasmas **21**, 090501 (2014).

[4] A. Loarte, G. Huijsmans, S. Futatani, L. Baylor, T. Evans, D. M. Orlov, O. Schmitz, M. Becoulet, P. Cahyna, Y. Gribov, A. Kavin, A. Sashala Naik, D. Campbell, T. Casper, E. Daly, H. Frerichs, A. Kischner, R. Laengner, S. Lisgo, R. Pitts, G. Saibene, and A. Wingen, "Progress on the application of ELM control schemes to ITER scenarios from the non-active phase to DT operation," Nucl. Fusion **54**, 033007 (2014).

[5] S. Jachmich, G. Arnoux, S. Brezinsek, S. Devaux, T. Eich, W. Fundamenski, C. Giroud, H. R. Koslowski, Y. Liang, E. de la Luna, G. Maddison, H. Thomsen, and JRT-EFDA Contributors, "Power and particle fluxes to plasma-facing components in mitigated-ELM H-mode discharges on JET," in *Proceedings of the 19th International Conference on Plasma-Surface Interactions in Controlled Fusion Devices, 2010* [J. Nucl. Mater. **415**, S894–S900 (2011)].

[6] J. Rapp, T. Eich, M. von Hellermann, A. Herrmann, L. C. Ingesson, S. Jachmich, G. F. Matthews, V. Philipps, G. Saibene, and Contributors to the EFDA-JET Workprogramme, "ELM mitigation by nitrogen seeding in the JET gas box divertor," Plasma Phys. Controlled Fusion **44**, 639–652 (2002).

[7] Y. Corre, E. Joffrin, P. Monier-Garbet, Y. Andrew, G. Arnoux, M. Beurskens, S. Brezinsek, M. Brix, R. Buttery, I. Coffey, K. Crombe, E. de La Luna, R. Felton, C. Giroud, S. Hacquin, J. Hobirk, A. Huber, F. Imbeaux, S. Jachmich, M. Kempenaars, X. Litaudon, H. Leggate, T. Loarer, G. Maddison, E. Rachlew, J. Rapp, O. Sauter, A. Savchkov, G. Telesca, A. Widdowson, K. D. Zastrow, O. Zimmermann, and JET-EFDA collaborators, "Hybrid H-mode scenario with nitrogen seeding and type III ELMs in JET," Plasma Phys. Controlled Fusion **50**, 115012 (2008).

[8] T. Rhee, J. M. Kwon, P. H. Diamond, and W. W. Xiao, "On the mechanism for edge localized mode mitigation by supersonic molecular beam injection," Phys. Plasmas **19**, 022505 (2012).

[9] W. Xiao, P. Diamond, X. Zou, J. Dong, X. Ding, L. Yao, B. Feng, C. Chen, W. Zhong, M. Xu, B. Yuan, T. Rhee, J. Kwon, Z. Shi, J. Rao, G. Lei, J. Cao, J. Zhou, M. Huang, D. Yu, Y. Huang, K. Zhao, Z. Cui, X. Song, Y. Gao, Y. Zhang, J. Cheng, X. Han, Y. Zhou, Y. Dong, X. Ji, Q. Yang, Y. Liu, Y. Lan, X. Duan, Y. Liu, and the HL-2A Team, "ELM mitigation by supersonic molecular beam injection into the H-mode pedestal in the HL-2A tokamak," Nucl. Fusion **52**, 114027 (2012).

[10] J. Kim, Y.-M. Jeon, W. Xiao, S.-W. Yoon, J.-K. Park, G. Yun, J.-W. Ahn, H. Kim, H.-L. Yang, H. Kim, S. Park, J. Jeong, M. Jung, G. Choe, W. Ko, S.-G. Lee, Y. Nam, J. Bak, K. Lee, H. Na, S.-H. Hahn, P. Diamond, T. Rhee, J. Kwon, S. Sabbagh, Y. Park, H. Park, Y. Na, W. Kim, J. Kwak, and the KSTAR Contributors, "ELM control experiments in the KSTAR device," Nucl. Fusion **52**, 114011 (2012).

[11] A. W. Degeling, Y. R. Martin, J. B. Lister, L. Villard, V. N. Dokouka, V. E. Lukash, and R. R. Khayrutdinov, "Magnetic triggering of ELMs in TCV," Plasma Phys. Controlled Fusion **45**, 1637–1655 (2003).

[12] M. Lennholm, D. Frigione, J. Graves, P. Beaumont, T. Blackman, I. Carvalho, I. Chapman, R. Dumont, R. Felton, L. Garzotti, M. Goniche, A. Goodyear, D. Grist, S. Jachmich, T. Johnson, P. Lang, E. Lerche, E. de la Luna, I. Monakhov, R. Mooney, J. Morris, M. Nave, M. Reich, F. Rimini, G. Sips, H. Sheikh, C. Sozzi, M. Tsalas, and JET Contributors, "Real-time control of ELM and sawtooth frequencies: Similarities and differences," Nucl. Fusion **56**, 016008 (2016).

[13] R. Maingi, T. H. Osborne, B. P. LeBlanc, R. E. Bell, J. Manickam, P. B. Snyder, J. E. Menard, D. K. Mansfield, H. W. Kugel, R. Kaita, S. P. Gerhardt, S. A. Sabbagh, and F. A. Kelly, "Edge-localized-mode suppression through density-profile modification with lithium-wall coatings in the national spherical torus experiment," Phys. Rev. Lett. **103**, 075001 (2009).

[14] R. Maingi, D. Boyle, J. Canik, S. Kaye, C. Skinner, J. Allain, M. Bell, R. Bell, S. Gerhardt, T. Gray, M. Jaworski, R. Kaita, H. Kugel, B. LeBlanc, J. Manickam, D. Mansfield, J. Menard, T. Osborne, R. Raman, A. Roquemore, S. Sabbagh, P. Snyder, and V. Soukhanovskii, "The effect of progressively increasing lithium coatings on plasma discharge characteristics, transport, edge profiles and ELM stability in the national spherical torus experiment," Nucl. Fusion **52**, 083001 (2012).

[15] H. W. Kugel, M. G. Bell, J. P. Allain, R. E. Bell, S. Ding, S. P. Gerhardt, M. A. Jaworski, R. Kaita, J. Kallman, S. M. Kaye, B. P. LeBlanc, R. Maingi, R. Majeski, R. Maqueda, D. K. Mansfield, D. Mueller, R. Nygren, S. F. Paul, R. Raman, A. L. Roquemore, S. A. Sabbagh, H. Schneider, C. H. Skinner, V. A. Soukhanovskii, C. N. Taylor, J. R. Timberlake, W. R. Wampler, L. E. Zakharov, and S. J. Zweben, "NSTX plasma response to lithium coated divertor," in *Proceedings of the 19th International Conference on Plasma-Surface Interactions in Controlled Fusion Devices, 2010* [J. Nucl. Mater. **415**, S400–S404 (2011)].

[16] P. Lang, J. Neuhauser, L. Horton, T. Eich, L. Fattorini, J. Fuchs, O. Gehre, A. Herrmann, P. Ignácz, M. Jakobi, S. Kálvin, M. Kaufmann, G. Kocsis, B. Kurzan, C. Maggi, M. Manso, M. Maraschek, V. Mertens, A. Mück, H. Murmann, R. Neu, I. Nunes, D. Reich, M. Reich, S. Saarelma, W. Sandmann, J. Stober, U. Vogl, and the ASDEX Upgrade Team, "ELM frequency control by continuous small pellet injection in ASDEX upgrade," Nucl. Fusion **43**, 1110–1120 (2003).

[17] P. Lang, A. Alonso, B. Alper, E. Belonohy, A. Boboc, S. Devaux, T. Eich, D. Frigione, K. Gál, L. Garzotti, A. Geraud, G. Kocsis, F. Köchl, K. Lackner, A. Loarte, P. Lomas, M. Maraschek, H. Müller, R. Neu, J. Neuhauser, G. Petravich, G. Saibene, J. Schweinzer, H. Thomsen, M. Tsalas, R. Wenninger, H. Zohm, and JET EFDA Contributors, "ELM pacing investigations at JET with the new pellet launcher," Nucl. Fusion **51**, 033010 (2011).

[18] Y. Liang, X. Z. Gong, K. F. Gan, E. Gauthier, L. Wang, M. Rack, Y. M. Wang, L. Zeng, P. Denner, A. Wingen, B. Lv, B. J. Ding, R. Chen, L. Q. Hu, J. S. Hu, F. K. Liu, Y. X. Jie, J. Pearson, J. P. Qian, J. F. Shan, B. Shen, T. H. Shi, Y. Sun, F. D. Wang, H. Q. Wang, M. Wang, Z. W. Wu, S. B. Zhang, T. Zhang, X. J. Zhang, N. Yan, G. S. Xu, H. Y. Guo, B. N. Wan, and J. G. Li, "Magnetic topology changes induced by lower hybrid waves and their profound effect on edge-localized modes in the EAST tokamak," Phys. Rev. Lett. **110**, 235002 (2013).

[19] T. E. Evans, R. A. Moyer, P. R. Thomas, J. G. Watkins, T. H. Osborne, J. A. Boedo, E. J. Doyle, M. E. Fenstermacher, K. H. Finken, R. J. Groebner, M. Groth, J. H. Harris, R. J. La Haye, C. J. Lasnier, S. Masuzaki, N. Ohyabu, D. G. Pretty, T. L. Rhodes, H. Reimerdes, D. L. Rudakov, M. J. Schaffer, G. Wang, and L. Zeng, "Suppression of large edge-localized modes in high-confinement DIII-D plasmas with a stochastic magnetic boundary," Phys. Rev. Lett. **92**, 235003 (2004).

[20] T. E. Evans, R. A. Moyer, K. H. Burrell, M. E. Fenstermacher, I. Joseph, A. W. Leonard, T. H. Osborne, G. D. Porter, M. J. Schaffer, P. B. Snyder, P. R. Thomas, J. G. Watkins, and W. P. West, "Edge stability and transport control with resonant magnetic perturbations in collisionless tokamak plasmas," Nat. Phys. **2**, 419–423 (2006).

[21] Y. Liang, H. R. Koslowski, P. R. Thomas, E. Nardon, B. Alper, P. Andrew, Y. Andrew, G. Arnoux, Y. Baranov, M. Bécoulet, M. Beurskens, T. Biewer, M. Bigi, K. Crombe, E. De La Luna, P. de Vries, W. Fundamenski, S. Gerasimov, C. Giroud, M. P. Gryaznevich, N. Hawkes, S. Hotchin, D. Howell, S. Jachmich, V. Kiptily, L. Moreira, V. Parail, S. D. Pinches, E. Rachlew, and O. Zimmermann, "Active control of type-I edge-localized modes with $n = 1$ perturbation fields in the JET tokamak," Phys. Rev. Lett. **98**, 265004 (2007).

[22] W. Suttrop, T. Eich, J. C. Fuchs, S. Günter, A. Janzer, A. Herrmann, A. Kallenbach, P. T. Lang, T. Lunt, M. Maraschek, R. M. McDermott, A. Mlynek, T. Pütterich, M. Rott, T. Vierle, E. Wolfrum, Q. Yu, I. Zammuto, and H. Zohm, "First observation of edge localized modes mitigation with resonant and nonresonant magnetic perturbations in ASDEX upgrade," Phys. Rev. Lett. **106**, 225004 (2011).

[23] Y. M. Jeon, J.-K. Park, S. W. Yoon, W. H. Ko, S. G. Lee, K. D. Lee, G. S. Yun, Y. U. Nam, W. C. Kim, J.-G. Kwak, K. S. Lee, H. K. Kim, and H. L. Yang, "Suppression of edge localized modes in high-confinement KSTAR plasmas by nonaxisymmetric magnetic perturbations," Phys. Rev. Lett. **109**, 035004 (2012).

21 July 2024 15:12:50

[24]A. Kirk, E. Nardon, R. Akers, M. Bécoulet, G. De Temmerman, B. Dudson, B. Hnat, Y. Liu, R. Martin, P. Tamain, D. Taylor, and the MAST Team, "Resonant magnetic perturbation experiments on MAST using external and internal coils for ELM control," Nucl. Fusion **50**, 034008 (2010).

[25]Y. Sun, Y. Liang, Y. Liu, S. Gu, X. Yang, W. Guo, T. Shi, M. Jia, L. Wang, B. Lyu, C. Zhou, A. Liu, Q. Zang, H. Liu, N. Chu, H. Wang, T. Zhang, J. Qian, L. Xu, K. He, D. Chen, B. Shen, X. Gong, X. Ji, S. Wang, M. Qi, Y. Song, Q. Yuan, Z. Sheng, G. Gao, P. Fu, and B. Wan, "Nonlinear transition from mitigation to suppression of the edge localized mode with resonant magnetic perturbations in the EAST tokamak," Phys. Rev. Lett. **117**, 115001 (2016).

[26]W. Suttrop, A. Kirk, R. Nazikian, N. Leuthold, E. Strumberger, M. Willensdorfer, M. Cavedon, M. Dunne, R. Fischer, S. Fietz, J. C. Fuchs, Y. Q. Liu, R. M. McDermott, F. Orain, D. A. Ryan, and E. Viezzer, "Experimental studies of high-confinement mode plasma response to non-axisymmetric magnetic perturbations in ASDEX upgrade," Plasma Phys. Controlled Fusion **59**, 014049 (2016).

[27]T. E. Evans, R. A. Moyer, J. G. Watkins, P. R. Thomas, T. H. Osborne, J. A. Boedo, M. E. Fenstermacher, K. H. Finken, R. J. Groebner, M. Groth, J. Harris, G. L. Jackson, R. J. L. Haye, C. J. Lasnier, M. J. Schaffer, G. Wang, and L. Zeng, "Suppression of large edge localized modes in high confinement DIII-D plasmas with a stochastic magnetic boundary," J. Nucl. Mater. **337–339**, 691–696 (2005).

[28]T. E. Evans, M. E. Fenstermacher, R. A. Moyer, T. H. Osborne, J. G. Watkins, P. Gohil, I. Joseph, M. J. Schaffer, L. R. Baylor, M. Bécoulet, J. A. Boedo, K. H. Burrell, J. S. deGrassie, K. H. Finken, T. Jernigan, M. W. Jakubowski, C. J. Lasnier, M. Lehnen, A. W. Leonard, J. Lonnroth, E. Nardon, V. Parail, O. Schmitz, B. Unterberg, and W. P. West, "RMP ELM suppression in DIII-D plasmas with ITER similar shapes and collisionalities," Nucl. Fusion **48**, 024002 (2008).

[29]Q. M. Hu, R. Nazikian, B. A. Grierson, N. C. Logan, J.-K. Park, C. Paz-Soldan, and Q. Yu, "The density dependence of edge-localized-mode suppression and pump-out by resonant magnetic perturbations in the DIII-D tokamak," Phys. Plasmas **26**, 120702 (2019).

[30]M. Becoulet, F. Orain, P. Maget, N. Mellet, X. Garbet, E. Nardon, G. T. A. Huysmans, T. Casper, A. Loarte, P. Cahyna, A. Smolyakov, F. L. Waelbroeck, M. Schaffer, T. Evans, Y. Liang, O. Schmitz, M. Beurskens, V. Rozhansky, and E. Kaveeva, "Screening of resonant magnetic perturbations by flows in tokamaks," Nucl. Fusion **52**, 054003 (2012).

[31]R. Fitzpatrick, "Theory of edge localized mode suppression by static resonant magnetic perturbations in the DIII-D tokamak," Phys. Plasmas **27**, 042506 (2020).

[32]R. Nazikian, C. Paz-Soldan, J. Callen, J. deGrassie, D. Eldon, T. Evans, N. Ferraro, B. Grierson, R. Groebner, S. Haskey, C. Hegna, J. King, N. Logan, G. McKee, R. Moyer, M. Okabayashi, D. Orlov, T. Osborne, J.-K. Park, T. Rhodes, M. Shafer, P. Snyder, W. Solomon, E. Strait, and M. Wade, "Pedestal bifurcation and resonant field penetration at the threshold of edge-localized-mode suppression in the DIII-D tokamak," Phys. Rev. Lett. **114**, 105002 (2015).

[33]C. Sung, G. Wang, T. L. Rhodes, S. P. Smith, T. H. Osborne, M. Ono, G. R. McKee, Z. Yan, R. J. Groebner, E. M. Davis, L. Zeng, W. A. Peebles, and T. E. Evans, "Increased electron temperature turbulence during suppression of edge localized mode by resonant magnetic perturbations in the DIII-D tokamak," Phys. Plasmas **24**, 112305 (2017).

[34]G. R. McKee, Z. Yan, C. Holland, R. J. Buttery, T. E. Evans, R. A. Moyer, S. Mordijck, R. Nazikian, T. L. Rhodes, O. Schmitz, and M. R. Wade, "Increase of turbulence and transport with resonant magnetic perturbations in ELM-suppressed plasmas on DIII-D," Nucl. Fusion **53**, 113011 (2013).

[35]R. A. Moyer, T. E. Evans, T. H. Osborne, P. R. Thomas, M. Becoulet, J. Harris, K.-H. Finken, J. A. Boedo, E. J. Doyle, M. E. Fenstermacher, P. Gohil, R. J. Groebner, M. Groth, G. L. Jackson, R. J. La Haye, C. J. Lasnier, A. W. Leonard,

G. R. McKee, H. Reimerdes, T. L. Rhodes, D. L. Rudakov, M. J. Schaffer, P. B. Snyder, M. R. Wade, G. Wang, J. G. Watkins, W. P. West, and L. Zeng, "Edge localized mode control with an edge resonant magnetic perturbation," Phys. Plasmas **12**, 056119 (2005).

[36]R. Hager, C. S. Chang, N. M. Ferraro, and R. Nazikian, "Gyrokinetic study of collisional resonant magnetic perturbation (RMP)-driven plasma density and heat transport in tokamak edge plasma using a magnetohydrodynamic screened RMP field," Nucl. Fusion **59**, 126009 (2019).

[37]S. Taimourzadeh, L. Shi, Z. Lin, R. Nazikian, I. Holod, and D. Spong, "Effects of RMP-induced changes of radial electric fields on microturbulence in DIII-D pedestal top," Nucl. Fusion **59**, 046005 (2019).

[38]R. S. Wilcox, A. Wingen, M. R. Cianciosa, N. M. Ferraro, S. P. Hirshman, C. Paz-Soldan, S. K. Seal, M. W. Shafer, and E. A. Unterberg, "Modeling of 3D magnetic equilibrium effects on edge turbulence stability during RMP ELM suppression in tokamaks," Nucl. Fusion **57**, 116003 (2017).

[39]F. M. Laggner, D. Eldon, A. O. Nelson, C. Paz-Soldan, A. Bortolon, T. E. Evans, M. E. Fenstermacher, B. A. Grierson, Q. Hu, D. A. Humphreys, A. W. Hyatt, R. Nazikian, O. Meneghini, P. B. Snyder, E. A. Unterberg, E. Kolemen, and the DIII-D Team, "Real-time pedestal optimization and ELM control with 3D fields and gas flows on DIII-D," Nucl. Fusion **60**, 076004 (2020).

[40]S. Kim, R. Shousha, S. Hahn, A. Nelson, J. Wai, S. Yang, J.-K. Park, R. Nazikian, N. Logan, Y. Jeon, Y. In, J. Lee, J. Kim, C. Lee, Y.-S. Na, and E. Kolemen, "Optimization of 3D controlled ELM-free state with recovered global confinement for KSTAR with n = 1 resonant magnetic field perturbation," Nucl. Fusion **62**, 026043 (2022).

[41]S.-h. Hahn, H. Han, M. H. Woo, J. G. Bak, J. Chung, Y. M. Jeon, J. H. Jeong, M. Joung, J. W. Juhn, H. S. Kim, H. Kim, M. W. Lee, G. W. Shin, T. H. Tak, S. W. Yoon, J. Barr, N. W. Eidietis, D. A. Humphreys, A. Hyatt, B. G. Penaflor, D. A. Piglowski, M. L. Walker, A. S. Welander, M. D. Boyer, K. Erickson, and D. Mueller, "Advances and challenges in KSTAR plasma control toward long-pulse, high-performance experiments," Fusion Eng. Des. **156**, 111622 (2020).

[42]H. K. Na, S. Sajjad, J. M. Park, and M. Kwon, "Configuration and installation design of optical diagnostic systems on KSTAR," Fusion Eng. Des. **86**, 66–70 (2011).

[43]H. Han, Y. Jeon, S. Hahn, H. Ahn, J. Bak, Y. In, J. Kim, M. Woo, H. Kim, J. Jin, B. Park, and S. Yoon, "Versatile controllability of non-axisymmetric magnetic perturbations in KSTAR experiments," Fusion Eng. Des. **108**, 60–66 (2016).

[44]H. K. Kim, H. L. Yang, G. H. Kim, J.-Y. Kim, H. Jhang, J. S. Bak, and G. S. Lee, "Design features of the KSTAR in-vessel control coils," in *Proceeding of the 25th Symposium on Fusion Technology* [Fusion Eng. Des. **84**, 1029–1032 (2009)].

[45]J.-K. Park, Y. Jeon, Y. In, J.-W. Ahn, R. Nazikian, G. Park, J. Kim, H. Lee, W. Ko, H.-S. Kim, N. C. Logan, Z. Wang, E. A. Feibush, J. E. Menard, and M. C. Zarnstroff, "3D field phase-space control in tokamak plasmas," Nat. Phys. **14**, 1223–1228 (2018).

[46]D. Eldon, E. Kolemen, J. Barton, A. Briesemeister, D. Humphreys, A. Leonard, R. Maingi, M. Makowski, A. McLean, A. Moser, and P. Stangeby, "Controlling marginally detached divertor plasmas," Nucl. Fusion **57**, 066039 (2017).

[47]J.-k. Park, A. H. Boozer, and A. H. Glasser, "Computation of three-dimensional tokamak and spherical torus equilibria," Phys. Plasmas **14**, 052110 (2007).

[48]Q. M. Hu, J.-K. Park, N. C. Logan, S. M. Yang, B. A. Grierson, R. Nazikian, and Q. Yu, "Nonlinear two-fluid modeling of plasma response to RMPs for the ELM control in the ITER baseline," Nucl. Fusion **61**, 106006 (2021).

[49]M. E. Fenstermacher, T. Abrams, K. Barada, J. L. Barr, L. Casali, X. Chen, C. Collins, S. Ding, B. A. Grierson, Q. Hu, A. Marinoni, A. G. McLean, C. Paz-Soldan, C. Petty, L. Schmitz, D. Shiraki, L. Wang, and T. M. Wilks, "DIII-D research advancing the physics basis for optimizing the tokamak approach to fusion energy," Nucl. Fusion (unpublished).